Research Article

Nano Research
2023, 16(8): 11528–11539

ISSN 1998-0124 CN 11-5974/O4
https://doi.org/10.1007/s12274-023-5876-7

Influence of structural defects on charge density waves in 1T-TaS_2

Iaroslav Lutsyk[1], Karol Szalowski[1] (✉), Pawel Krukowski[1], Pawel Dabrowski[1], Maciej Rogala[1], Witold Kozlowski[1], Maxime Le Ster[1], Michal Piskorski[1], Dorota A. Kowalczyk[1], Wojciech Rys[1], Rafal Dunal[1], Aleksandra Nadolska[1], Klaudia Toczek[1], Przemyslaw Przybysz[1], Ewa Lacinska[2], Johannes Binder[2], Andrzej Wysmolek[2], Natalia Olszowska[3,4], Jacek J. Kolodziej[3,4], Martin Gmitra[5,6], Takuma Hattori[7], Yuji Kuwahara[7], Guang Bian[8], Tai-Chang Chiang[9], and Pawel J. Kowalczyk[1] (✉)

[1] *Faculty of Physics and Applied Informatics, University of Lodz, Pomorska 149/153, 90-236 Lodz, Poland*
[2] *Faculty of Physics, University of Warsaw, Pasteura 5, 02-093 Warsaw, Poland*
[3] *Faculty of Physics, Astronomy, and Applied Computer Science, Jagiellonian University, Lojasiewicza 11, 30-348 Krakow, Poland*
[4] *National Synchrotron Radiation Centre SOLARIS, Jagiellonian University, Czerwone Maki 98, 30-392 Kraków, Poland*
[5] *Institute of Physics, Faculty of Science, Pavol Jozef Šafárik University in Košice, Park Angelinum 9, 040 01 Košice, Slovakia*
[6] *Institute of Experimental Physics, Slovak Academy of Sciences, Watsonova 47, 040 01 Košice, Slovakia*
[7] *Department of Precision Engineering, Graduate School of Engineering, Osaka University, 2-1 Yamada-oka, Suita 565-0871, Japan*
[8] *Department of Physics and Astronomy, University of Missouri, Columbia, Missouri 65211, USA*
[9] *Department of Physics and Frederick Seitz Materials Research Laboratory, University of Illinois at Urbana-Champaign, Urbana, Illinois 61801-3080, USA*

Received: 18 March 2023 / **Revised:** 22 May 2023 / **Accepted:** 30 May 2023

ABSTRACT

The influence of intrinsic defects of 1T-TaS_2 on charge density waves (CDWs) is studied using scanning tunneling microscopy and spectroscopy (STM, STS), angle-resolved photoelectron spectroscopy (ARPES), and density functional theory (DFT). We identify several types of structural defects and find that most have a local character limited to a single CDW site, with a single exception which effectively behaves as a dopant, leading to band-bending and affecting multiple neighboring sites. While only one type of defect can be observed by STM topographic imaging, all defects are easily resolved in STS mapping. Our results indicate modulation of the Mott band gap commensurate with the CDW and breaking of the three-fold symmetry of electronic states. DFT calculations (with included Coulomb interactions) are used to investigate the electronic structure, focusing on both sulfur vacancy and oxygen-sulfur substitution. The sulfur vacancy system, characterized with a metallic behavior, is identified as the origin of one of the experimentally observed defects. Additionally, the effect of oxidation of 1T-TaS_2 depends on the substitution site, leading to the heterogeneity of electronic properties.

1 Introduction

It is known that crystalline defects alter the properties of materials [1–3]. The prime example is n- and p-doping of silicon which have become the foundation of the modern semiconductor industry [4, 5]. With gate sizes downscaled to below 10 nm [6, 7] new materials are expected to take over in order to sustain the global need for electronic device miniaturization [7]. Materials with reduced geometry hold promise in that regard, such as two-dimensional (2D) crystals, which can lead to further miniaturization of electronic components [7–10] and accompany the emergence of the next-generation optoelectronic devices [11, 12]. In these systems, the active layer has a thickness of several angstroms, and therefore even a single point defect can severely alter the device properties, leading to either improvements or deteriorations. It is thus crucial to understand the naturally existing defects in a variety of 2D materials to exploit their properties in the future. When the study of 2D materials is limited by their high reactivity [13], their properties are often investigated through their layered bulk counterparts, in which single layers are held together by weak van der Waals (vdW) forces.

Among the growing family of vdW materials, binary compounds of transition metal dichalcogenides (TMDCs) are one of the most interesting ones thanks to the variety of their forms and polytypes. In particular, 1T-TaS_2 is of special interest due to its complex phase diagram [14–17] related to periodic lattice distortion (PLD) [14] associated with the emergence of emergence of charge density waves (CDW), Mott band gap formation, and metal to insulator transition at reduced temperatures [17]. Theoretical results show that Coulomb interactions between electrons lead to non-zero local magnetization [18], but experimental detection of its magnetic properties is a challenge, due to spin frustration effects [19]. It was recently shown that stacking faults leading to different mutual arrangements of PLDs in two-layer 1T-TaS_2 are responsible for considerable variations of its electronic structure resolved by scanning tunneling microscopy (STM) [20]. Modification of its electronic properties associated with the phase transitions was also achieved by STM pulses [21] or laser irradiation [22–25]. In another study, Raman optical activity was shown in bulk 1T-TaS_2 [26], suggesting the presence of chiral phases in this material. Chiral properties were also studied as an

Address correspondence to Karol Szalowski, karol.szalowski@uni.lodz.pl; Pawel J. Kowalczyk, pawel.kowalczyk@uni.lodz.pl

effect of Ti doping [27, 28]. Moreover, Se doping of 1T-TaS_2 promotes the emergence of a superconducting phase [29]. Interestingly, sulfur vacancies healed by oxygenation were found to enhance superconductivity in 2H-TaS_2 [13].

In this paper, we focus on point defects in 1T-TaS_2 by using STM measurements, complemented by density functional theory (DFT) simulations. We attribute the protrusions in the atomic resolution images of the defect-free surface as related to sulfur in the top layer of 1T-TaS_2, a conclusion that is confirmed by DFT calculations. In turn, our scanning tunneling spectroscopy (STS) measurements which resolve the tunneling conductance (TC, calculated as first derivative of current by bias voltage, i.e., dI/dV) allow us to observe a number of CDW modifications ascribed to electron–electron interactions. Interestingly, these changes break the three-fold symmetry expected for 1T-TaS_2 which potentially indicates the existence of chirality in this material [26, 30, 31]. We also observe a modulation of lower and higher Hubbard bands (LHB and HHB) associated to the formation of the PLD, which was associated to a modulation of the Mott band gap. dI/dV images recorded in the vicinity of the Fermi level indicate the presence of several types of defects with varying local density of states (LDOS) profiles, compared to defect-free 1T-TaS_2. One of these defects labeled D1 behaves as an acceptor, affecting a region of several nanometers in its vicinity. Since the density of this type of defect is relatively large in our samples, the surface potential is highly modulated, leading to considerable fluctuations in the position of LHB and HHB. Another defect attributed to sulfur vacancy (labeled D2) leads to closure of the Mott band gap and emergence of local metallic properties of 1T-TaS_2. The spectroscopic features associated to other types of defects are more subtle and are related to either a slight shift of LHB or CDW amplitude modulation at particular energies in dI/dV data. The experimentally observed defects are difficult to simulate due to the complex structure of 1T-TaS_2. Therefore, a qualitative model involving only a monolayer and two kinds of structural defects is explored here to capture essential physics of the complex structure. Namely, we use DFT and DFT + U (which includes Coulomb interactions between Ta 5d orbitals [28, 32]) to calculate the properties of defect-free 1T-TaS_2, sulfur vacancies, and their substitution by oxygen atoms. Our unfolded band structure calculations for the defect free system are compared to ARPES data, showing good agreement. Based on our calculations of defects in 1T-TaS_2, we believe that the local metallic behavior observed experimentally results from sulfur vacancies. We also show the electronic property heterogeneity for different sulfur sites substituted by oxygen, i.e., either semiconducting properties with preserved magnetization or metallic behaviour with considerably hindered effective magnetization. These results clearly indicate that the presence of defects in 1T-TaS_2 will be crucial for subsequent fundamental studies of this material and further device design.

2 Results

2.1 1T-TaS_2 atomic structure

1T-TaS_2 is a vdW crystal where single layers are composed of three sheets of atoms: S–Ta–S held by covalent bonds (see Fig. 1(a)). PLD forms as a result of electron–electron interaction at low temperatures, leading to a distortion of the Ta sublattice (see blue arrows in Fig. 1(b)) [33]. The central, undistorted atom (A-Ta in Fig. 1(b)) is surrounded by six Ta atoms (labeled B) which are shifted by the same amount towards the A-Ta atom. Six second nearest-neighbor Ta atoms (labeled C) undergo an even stronger distortion towards the A-Ta. These thirteen Ta atoms form a geometric figure called hexagram (from Greek) or sexagram (from Latin), also known as David Star [33] (see Fig. 1(b)). The geometry of the David Stars allows the formation of CDW/PLD chiral superstructure in two equivalent directions [25, 34]. As a consequence of the PLD, the unit cell of 1T-TaS_2 (indicated using black rhombus) is considerably larger than in the undistorted case. This results in reduction of the first Brillouin zone as shown in inset of Fig. 1(b), requiring unfolding of the calculated electronic band structures (see the discussion below).

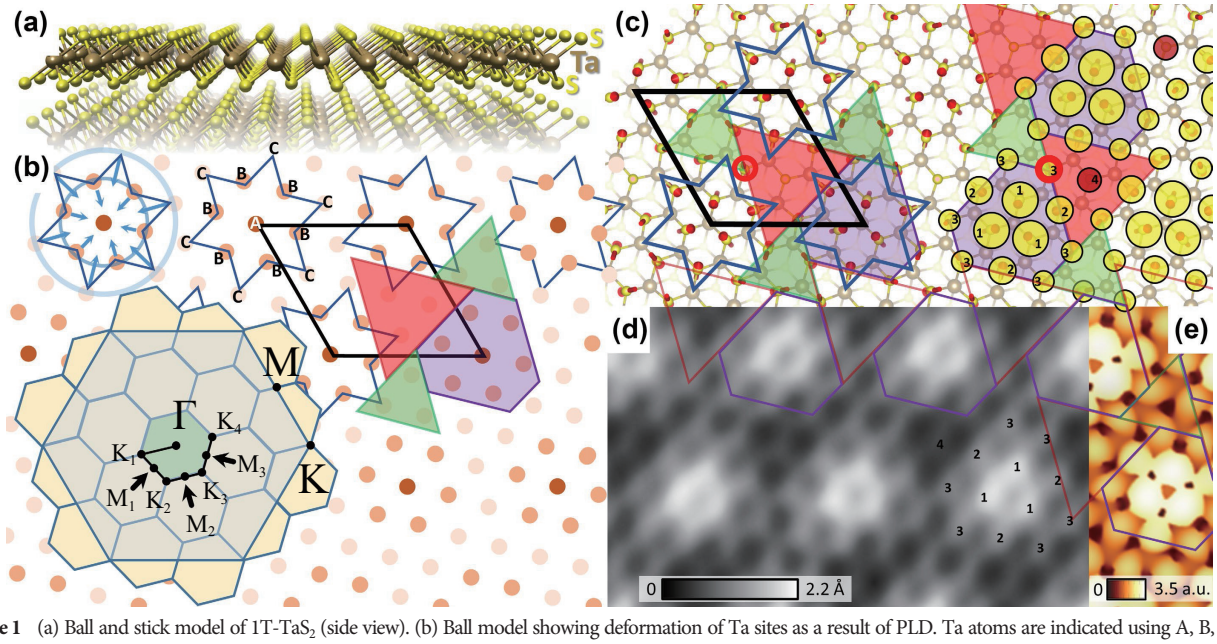

Figure 1 (a) Ball and stick model of 1T-TaS_2 (side view). (b) Ball model showing deformation of Ta sites as a result of PLD. Ta atoms are indicated using A, B, and C labels. Inset shows first Brillouin zone for 1T-TaS_2 and supercell. Path used to extract band diagrams shown in Fig. S8 in the ESM is indicated using black line. (c) Ball and stick model of 1T-TaS_2 (top view) with top sulfur and middle tantalum atoms shown. Red arrows represent direction and magnitude of top layer S atoms shift in consequence of PLD formation. Yellow and red rings indexed 1–4 indicate locations of S atoms. Radius of rings corresponds to the out-of-plane shift of S atoms. Red ring indicates S site for which DFT calculations are done. (d) High resolution STM image (2 V, 50 pA) showing atomic resolution and CDW recorded at 80 K. Characteristic atomic sites are enumerated 1–4. Scale bar in (d) corresponds to 1 nm. Black (white) corresponds to low (high) topographic height. (e) DFT simulated STM image (constant current, 0.1 V). The red and green triangles together with purple equiangular hexagons represent tiling the surfaces in ((b)–(d)).

The PLD is well reproduced in DFT calculations carried out for a single layer of 1T-TaS_2. The structural model in our DFT calculations is shown in Fig. 1(c) where top and bottom layer S atoms are indicated using different shades of yellow (pale yellow used for bottom layer). The red arrows represent the displacement vector affecting individual S atoms in the unit cell (located in the top layer). Our calculations show that the displacements of Ta atoms are mainly occurring in-plane, in contrast to the S atoms which distort along out-of-plane directions.

A high-resolution STM image of the 1T-TaS_2 surface is shown in Fig. 1(d), and Fig. 1(e) depicts a DFT simulated one. Both images are very similar, which indicates that protrusions can be ascribed to a higher LDOS above S atoms (see also our calculations discussed below). Note, in the published reports often atomic protrusions resolved in STM images are sometimes ascribed to Ta atoms [35], which is likely related to the STM tip condition [36], resulting in image inversion (Fig. 1) [37–40]. STM image shown in Fig. 1(d) is characterized by a clear CDW modulation (as a result of PLD formation), which is further modulated by protrusions corresponding to individual S atoms. Inspection of the CDW centers in Fig. 1(d) reveals the presence of three protrusions arranged in a triangle (labelled 1). These three protrusions correspond to three top layer S atoms, nearest neighbors of A-Ta, which are shifted out of the plane (with the highest magnitude indicated by arrows in Fig. 1(c)). They are indicated in Fig. 1(c) using yellow rings labelled 1 (short for 1-S). Note, the diameter of the rings shown in Fig. 1(c) corresponds to the relative distance of S atoms to the Ta plane, i.e., a larger ring diameter indicates S atom located further away from their initial position.

Three 1-S atoms in Fig. 1(d) are surrounded by nine protrusions forming an equiangular hexagon (shown in purple in Figs. 1(b)–1(d)) with a longer edge twice the length of the shorter one [41], i.e., spirolateral $2_{120°}$ [42] characterized by D_3 symmetry. In the center of longer edge of this hexagon, a slightly brighter protrusion is measured in STM images (see Fig. 1(d)). This protrusion corresponds to 2-S atom (see Fig. 1(c)) which also results from an out-of-plane displacement, yet with magnitude lower than that of the 1-S atoms. The remaining six S atoms (labeled 3-S) are shifted below the initial S plane and are located at the corners of the equiangular hexagon. Note, the equiangular hexagon and the David Star, both located at the corner of the unit cell (see Figs. 1(b) and 1(c)) are concentric (indicating that the net in-plane displacements of both S and Ta atoms are zero). Inspection of the structural model shown in Fig. 1(c) reveals that atoms belonging to three neighboring CDWs form an equilateral triangle with three 3-S atoms on each edge (green triangle in Figs. 1(c) and 1(d)). This triangle contains three C-Ta atoms which are the most distorted. Clearly, these 3-S atoms are imaged as three dips in STM images (see Fig. 1(d)). The protrusion seen in experimental data is a result of overlap of states density related to three 3-S atoms located at its edges. Three remaining C-Ta atoms are imaged by STM as even larger dips and are located in a region indicated with the red triangle in Fig. 1. A single 4-S atom is located at its center. Despite the very large displacement of the nearest neighbor C-Ta atoms, the 4-S atom remains nearly in its original position. It is imaged by STM as a weak protrusion located in the center of the red triangles (see Fig. 1(d)). These three geometric shapes used to describe the surface S atoms (red and green triangles, purple equiangular hexagon) periodically tile the surface of 1T-TaS_2. Figure S1 in the Electronic Supplementary Material (ESM) shows a similar tiling for the bottom surface of single-layer 1T-TaS_2 which is different in virtue of symmetry [26].

2.2 Scanning tunneling spectroscopy studies of defect-free 1T-TaS_2

Figure 2(a) shows a STM topography image of the CDW formed on 1T-TaS_2. This image was recorded together with a stack of dI/dV images obtained at different energies. The CDW shown in Fig. 2(a) looks uniform on a large area of the sample with only one distinct CDW site (characterized by lower apparent height) indicated D1 in Fig. 2(a). The fast Fourier transformation (FFT) of this STM image (see Fig. 2(b)) is characterized by the presence of three features (indicated as q1, q2, and q3), corresponding to real space periodicities. Based on q1–q3 features, CDW wavelength can be extracted and varies between 1.2–1.4 nm. Note, the D1 defect density estimated from a large-scale STM images (see inset in Fig. 2(c)) is at the level of 0.013 defect/nm^2 i.e., roughly 1 defect per surface area of 9 nm × 9 nm.

A typical dI/dV plot recorded at a CDW site (i.e., above the central A-Ta atom) is shown in Fig. 2(c). Its general shape, as well as the energy width of the Mott gap (0.4 eV) and the position of the LHB and HHB at –0.35 and 0.08 eV respectively [33] indicates T_A stacking, i.e., where the centres of successive David Stars in the

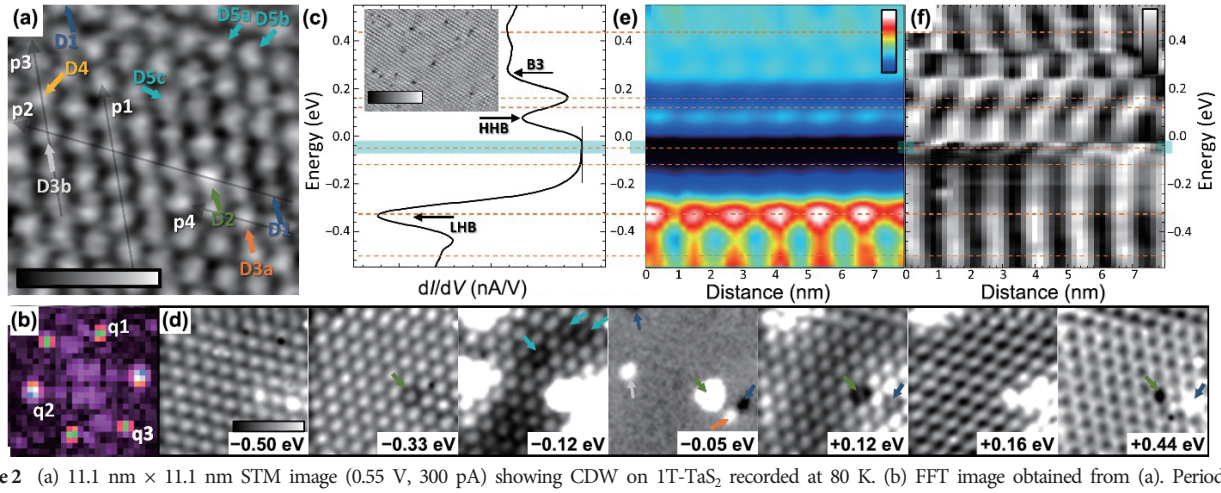

Figure 2 (a) 11.1 nm × 11.1 nm STM image (0.55 V, 300 pA) showing CDW on 1T-TaS_2 recorded at 80 K. (b) FFT image obtained from (a). Periodicities corresponding to CDW are indicated using labels q1–q3. (c) Typical tunneling conductance dI/dV plot recorded far from defects. Vertical line indicates zero value of dI/dV. (d) dI/dV images recorded at different energies extracted from dI/dV stack. (e) dI/dV waterfall plot recorded along black line p1 shown in (a). (f) dI/dV waterfall plot after normalization. Small arrows in ((a) and (d)) indicate location of defects labeled D1–D5. Arrows labeled p1–p4 indicate cross-section lines used to extract dI/dV waterfall plots shown in ((e) and (f)) and Figs. 4 (b)–4(d). Horizontal lines in ((c), (e), and (f)) indicate energies at which dI/dV images shown in (d) were recorded. Shaded regions in ((c), (e), and (f)) show band gap without clear CDW states. Inset in (c) 50 nm × 35 nm STM image (0.003 V, 1 nA, 80 K) showing defects on 1T-TaS_2. Scale bars in ((a) and (d)) correspond to 5 nm while in (c) to 20 nm.

1T-TaS_2 monolayers are aligned [20]. The assymetric location of HHB and HHB in respect to the Fermi level suggests n-doping of our crystals. Above the HHB, a clear minimum is observed and followed by a plateau extending until the end of the scan range, i.e., 0.55 eV. At the beginning of the plateau, a low amplitude maximum labeled B3 is located at approximately 0.29 eV followed by another one located at approximately 0.43 eV. This pattern, i.e., the HHB followed by minimum and plateau with two weak maxima is characteristic of 1T-TaS_2 [43].

By examining dI/dV images one can analyze spatial changes in the TC data at constant energy. A few dI/dV images obtained at different energies are shown in Fig. 2(d) (energy indicated on the bottom right, see also Fig. S2 in the ESM and Movie ESM1 where each frame corresponds to dI/dV image recorded at different energy). It is clear that the CDW periodicity is visible in each of these dI/dV images. Considerable changes in dI/dV mappings are noticeable across different energies. In particular, for energies up to 0.12 eV, the TC maxima have an oval shape and are centered at 1-S atoms (see Fig. 1(a)). The shape of ovals changes slightly at −0.50 and −0.33 eV, where an initially circular TC region evolves into elongated ones. This is an unexpected breaking of the three-fold symmetry in 1T-TaS_2. While non-ideal tip symmetries could partly explain these effects, we speculate that this phenomenon is related to an interlayer interaction associated with the chirality in these systems, first described for $TaSe_2$ [31] and recently confirmed in 1T-TaS_2 [26, 30].

A dramatic change in Fig. 2(d) is observed in the dI/dV maps recorded at 0.12 and 0.16 eV where within only 0.04 eV, the well-developed protrusions centered at 1-S atoms, are modified into a chicken net-like structure with protrusions moving off the 1-S atoms location. This structure is further modified as shown in dI/dV image recorded at 0.44 eV (see Fig. 2(d)). At this energy, dI/dV maxima (minima) are located at centers of green and red triangular tiles (over 1-S atoms) shown in Fig. 1(c). In consequence, the hexagonal dI/dV maxima form surrounding central equiangular hexagon with 1-S atoms located exactly in the center. Closer inspection of these data also reveals that slightly larger dI/dV values are located at every second corner of the hexagon (see 0.44 eV in Fig. 2(d)) and this is attributed to the different atomic arrangement in red and green tiles. Unfortunately, based only on our experimental results, we are not able to determine with certainty if the larger TC at 0.44 eV is centered at the red (thus at the location of 4-S atoms) or green tile due to limited lateral resolution during STS measurements. It is worth pointing out that the dI/dV dynamics described here are not only limited to 1T-TaS_2 but also observed in similar systems, e.g., 1T-$TaSe_2$ [44] and 1T-$NbSe_2$ [45].

Analysis of dI/dV images has the advantage (over dI/dV plots) to highlight subtle localized differences in TC, even for energies expected to be featureless. Data shown in Fig. 2(d) and Fig. S2 in the ESM suggest that the LDOS modulation in dI/dV images is also present in the Mott gap and vanishes only for a narrow energy range (−0.02, −0.07) eV (see cyan shaded region in Fig. 2(c)). The presence of such TC modulation is counterintuitive, but it has been reported in the Refs. [28, 35]. We attribute the non-zero LDOS in the Mott gap to the thermal smearing of the electronic structure (T = 80 K in our experiments), which is consistent with LHB and HHB states expanding toward the Fermi level, effectively reducing the gap.

Importantly, the presence of TC modulation is hidden in the Mott gap due to the color scale (see featureless black stripe along cyan marks in Fig. 2(e) recorded along the black arrow labelled p1 in Fig. 2(a)). To shed light onto the TC modulation within the Mott gap, we normalize every horizontal line of Fig. 2(e) to the [0, 1] range. The result of this normalization is shown in Fig. 2(f) and allows to see the dynamics and lateral offset change and contrast inversions of the CDW features across the investigated energy range. Indeed, in the range of (−0.02, −0.07) eV, the periodicity is highly distorted (indicating the lack of CDW modulation of LDOS at this energy, which is evident in Fig. 2(d) at −0.05 eV). The long-range periodicity also vanishes just below the B3 maximum at 0.24 eV and above B3 at approximately 0.35 eV. Interestingly, a smooth phase shift in the dI/dV waterfall plot can be observed for energies between HHB and B3. Within a thin narrow energy range, the CDW-driven TC modulations are laterally shifted and change shape from ovals toward chicken net-like pattern. Subtle TC modulation offset is also observed below −0.20 eV (see Fig. 2(f)), although less significantly. These observations are consistent with dI/dV images (shown in Fig. 2(d) and Fig. S2 in the ESM). Observed shifts of the TC maxima are further analyzed in DFT section below.

In Fig. 3, we present a more detailed analysis of the electronic structure landscape characteristic of 1T-TaS_2. Figure 3(a) shows both dI/dV spectra recorded over the CDW maxima and in the valleys between them. In general, the shape of both spectra is similar, however the TC at CDW maxima has a larger TC almost everywhere in the investigated energy range. This trend changes only for energies larger than 0.36 eV, where a contrast inversion occurs. In this regime, TC measured in the CDW valleys dominates over the initial CDW maxima sites (A-Ta). The dI/dV image obtained at +0.44 eV shown in Fig. 2(d) also highlights the contrast inversion.

A closer inspection of Fig. 3(a) reveals a slight variation of the LHB energy location, i.e., LHB measured between CDW sites is slightly shifted toward the Fermi energy when compared to the LHB position measured on top of CDW sites. In order to track the evolution of the LHB and HHB states, we measure their energy location, plotted as spatially resolved maps shown in Figs. 3(b) and 3(c) corresponding to LHB and HHB maximum location respectively (shades of gray represent energy location of the maximum in each pixel of the image). In both maps, one can see that energy position of LHB and HHB change considerably, i.e., by approximately 0.15 and 0.10 eV, respectively. We will discuss these changes later. Beside these significant energy shifts, a faint modulation of both LHB and HHB energies is also observed, which is clearly commensurate with the CDW seen in the topographic image (see Fig. 2(a)). The amplitude of modulation is lower for LHB (see Fig. 3(b)), where less distinct right diagonal stripes can be observed, corresponding to CDW valley sites. This color contrast is in line with dI/dV plot (Fig. 3(a)), indicating a shift toward the Fermi level of the LHB maxima measured in CDW valleys. In contrast, the HHB maximum shifts toward the Fermi energy for regions measured at CDW maxima and out of the Fermi energy for regions located in CDW valleys (see pattern shown in Fig. 3(c) in which spaces between CDWs are lighter, i.e., they are located closer to the Fermi level). These data show that both LHB and HHB maxima shift in registry, i.e., LHB and HHB shift toward and outward the Fermi level by the same amount. This is made evident in the Mott gap (Δ_{Mott} = HHB − LHB) map shown in Fig. 3(d), calculated for each pixel. At first sight, the image is relatively uniform without CDW-driven modulation, indicating that the observed shifts of LHB and HHB are indeed consistent.

In Fig. 3(e), we show histograms of the LHB and HHB energy locations. Both histograms are asymmetric with heavier tails on the right. These distributions reflect the LHB and HHB shifts discussed above. In Fig. 3(e), we also show a histogram of Mott gap width. The histogram is now symmetric, further confirming that LHB and HHB are correlated. The tails observed in both states nearly completely cancel out and the Mott gap width is equal to approximately 0.4 eV observed all over the surface (except

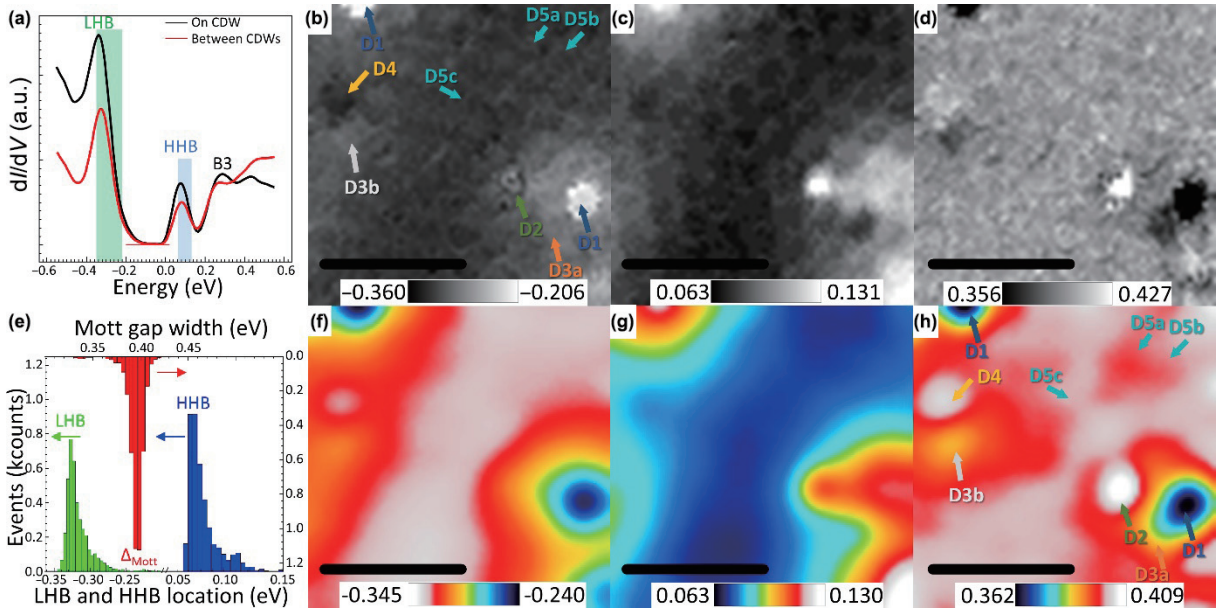

Figure 3 (a) Tunneling conductance plot recorded over STM-observed CDW maxima (black) and between them (red). (b) Spatial distribution of LHB energy location extracted from STS measurements conducted over region shown in Fig. 2(a). (c) Spatial distribution of HHB energy location. (d) Mott gap calculated as a difference between ((c) and (b)). (e) Histograms of LHB and HHB locations and Mott gap width. (f)–(h) Gaussian blurred LHB, HHB, and Mott gaps in ((b)–(d)), respectively. Green and blue bars in (a) show spread of LHB and HHB respectively. Arrows and labels in ((b) and (h)) indicate defect locations. Scale bars in ((b)–(d)) and ((f)–(h)) correspond to 5 nm.

for several regions discussed below). The estimated value of Δ_{Mott} here is in agreement with previous literature [20].

2.3 Scanning tunneling spectroscopy studies of defects in 1T-TaS_2

We now turn to discussing the effect of defects on the LHB and HHB states both at the location of the defect and within their local environment. In Figs. 3(b) and 3(c), the LHB, HHB, and Δ_{Mott} maps indeed show localized inhomogeneities. These can be better seen in the Gaussian-blurred images shown in Figs. 3(f)–3(h) corresponding to LHB, HHB, and Δ_{Mott} respectively. In these images, the extended color scale allows to emphasize these variations in the dI/dV data. Both LHB and HHB energies are generally invariant across large areas in Figs. 3(f) and 3(g) corresponding to pristine 1T-TaS_2 (note that the color scales in Figs. 3(f) and 3(b) are inverted so as to indicate energies away from the Fermi level). In contrast, the HHB and LHB energies vary considerably in the left and bottom-right of the images (see Figs. 3(f) and 3(g)). Clearly, these areas include several types of TaS_2 defects (labelled D1–D5), as indicated with arrows in Figs. 2(a) and 2(d) and Figs. 3(b) and 3(h). Defect D1 induces an increase of the LHB energy in a region of approximately 4 nm around its location. In our opinion, the two D1 defects separated by 7–8 nm are responsible for the positive LHB band-bending LHB in the left side of the map (one D1 defect is on the top left of Fig. 3(f); the second one is located on the left beyond the scan range). Defect D1 also induces an increase of the HHB state in a comparable region of influence. These two shifts cancel each other out in regions located a few nanometers away of D1, and as a consequence the Mott gap value (Figs. 3(d) and 3(h)) remains constant. This can be observed by comparing bottom left corner of Figs. 3(f)–3(h). In LHB and HHB maps, another type of defect labelled D2 can also be observed, which is better seen in STS maps (see Figs. 3(b) and 3(c)) rather than in smoothed versions (Figs. 3(f) and 3(g)). Signatures of D3 and D4 can be also noticed in these data. However, it is in the Mott gap image shown in Figs. 3(d) and 3(h) that most defects can be resolved. This shows that point-defects in 1T-TaS2 alter the Mott gap. The changes in Δ_{Mott} have a rather local nature and are limited to a single defected CDW site for most defects except for D1, which affects a region extending to several nanometers.

Further insight into the electronic structure of point defects can be extracted from the dI/dV plots shown in Fig. 4(a), as well as the dI/dV waterfall plots extracted along the line profiles of Fig. 2(a). In particular, the line p2 crosses three different defects D1, D2, and D3b (see dI/dV waterfall plot in Fig. 4(b)). At the location of D1, the LHB shifts toward while HHB outward the Fermi level. At the same time, the Mott gap is reduced by 0.04 eV to reach approximate Δ_{Mott}^{D1} = 0.36 eV. A closer inspection of the STM topographic image shown in Fig. 2(a) reveals that the apparent height (measured in constant-current mode) of the D1-CDW (i.e., CDW maximum associated to D1 defect) is considerably lower than the surrounding ones. The TC at the location of D1 is characterized with a prominent LHB feature and B1 features (B1 is the TC maximum located at 0.50–0.60 eV below the Fermi level; see Lutsyk et al. [33]), as shown in Fig. 4(a), and in the dI/dV waterfall plot shown in Fig. 4(b). As discussed above, the presence of D1 affects the electronic structure of the CDW in its neighborhood, i.e., the shift of the LHB energy towards the Fermi level can occur even 2–3 times the CDW's characteristic length away. Also, HHB is affected and shifted outward the Fermi level but to a less extent than LHB. In consequence, the Mott gap is narrower not only at D1 but also in its direct proximity (within a radius of ~ 1 nm). This is visible in the Mott gap energy map shown in Figs. 3(d) and 3(h). Note, however, the region around D1 that undergoes a Mott gap modification is more localized while LHB and HHB mutual shifts are more long range (as observed in the data shown in Figs. 3(f)–3(h)). This observation is consistent with D1 acting as an acceptor, resulting in band-bending in its neighborhood [46]. Based on the results shown in Fig. 4(b), we estimate the surface potential associated with D1 to be 0.1 eV, which also indicates the formation of a dipole on the surface [47]. The depletion region extends 4–5 nm away of D1.

The defect labeled D2 has a different nature to D1. Most importantly, it has a metallic character with a TC peak located just 0.03 eV below the Fermi level (see Figs. 4(a) and 4(b)). We speculate that this peak is the HHB, which was pushed towards low energies by 0.10 eV from its original position. It is supported

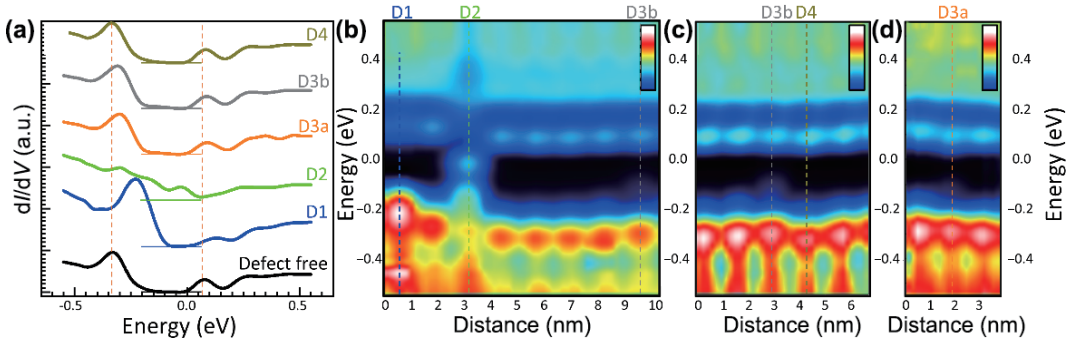

Figure 4 (a) Tunneling conductance plots recorded over defect-free and defected CDW sites. Plots are shifted vertically. The zero level is indicated by horizontal lines. Tunneling conductance dI/dV waterfall plots extracted along cross-section lines p2, p3, and p4 (shown in Fig. 2(a)) in ((b), (c), and (d)) respectively.

by the shape of D2 dI/dV plot (see Fig. 4(a)) for energies above the Fermi level. One can see three characteristic features typical for this energy range, i.e., a minimum and a plateau with two maxima. These features are typically preceded by the HHB maximum. These are visible in the D2 dI/dV plot (as mentioned above), and thus attribute these to the HHB. Noticeably, for dI/dV plot recorded over D2, a maximum can be observed at roughly the same energy position as LHB in defect-free 1T-TaS_2 (shifted up toward the Fermi level by a mere 0.03 eV) but with a considerably lower amplitude (see Figs. 4(a) and 4(b)). The observed energy shift is the result of band-bending caused by the neighboring D1, which is consistent with the data shown in the dI/dV waterfall plot (Fig. 4(b)), where all features in the vicinity of D1-LHB maxima (including D2-LHB) shift towards the Fermi level with a magnitude decreasing with the distance to the D1 defect. The Mott gap is equal to 0.27 eV and is characterized by the presence of an additional maximum seen as a shoulder approximately 0.12 eV above the LHB and 0.16 eV below the HHB (maximum location is equal to −0.14 eV). Finally, D2 is characterized with a slightly higher STM apparent height in its CDW center than other CDW sites (for a bias of +0.55 V). In our experiments, this defect is the only one that results in a protrusion in the STM topography data, meaning that tracking such defects in topographic mode is also possible. In contrast to D1, our data do not allow us to estimate the density of these defects on the 1T-TaS_2 surface. However, our data suggests a significantly lower D2 defect density than for D1.

The line profile p2 (Fig. 2(a)) also intersects another defect labeled D3b (see Figs. 4(a) and 4(b)). The same defect is also intersected along the p3 line (see Fig. 4(c)). Another defect of the same type, labeled D3a, is intersected by the p4 line (see Figs. 4(a) and 4(d)). The general electronic structure associated with the D3-type defects is in the first approximation very similar to that of defect-free 1T-TaS_2 (see Fig. 4(a) and Fig. S3 in the ESM). The main difference is the presence of a shoulder at approximately −0.12 eV (see Fig. S3 in the ESM and also blueish region in the Mott gap region in Figs. 4(b)–4(d)). Since D3 defects have an energy footprint located within the Mott gap, dI/dV maps can be used to identify them. One of such images recorded at −0.05 eV is shown in the set depicted in Fig. 2(d). Both D3 defects are observable as bright (large TC value) regions in the image, i.e., they have a non-zero TC in the Mott gap. Our experimental results also indicate that the LHB energy at the location of the D3 defect is slightly shifted upward, i.e., toward the Fermi level (see Figs. 3(b), 4(b), and 4(c) and Fig. S3 in the ESM). Note that the existence of D3 defects can be still tracked in dI/dV data in which tip electronic structure dominates below the Fermi level (i.e., LHB intensity is considerably decreased or even completely washed out). Usually, in such measurements, TC in vicinity to Mott band gap is slightly larger even if shoulder (as data shown here) is absent.

The LHB mapping (Fig. 3(b)) evidences an additional defect type, labeled as D4 (see dI/dV plot in Fig. 4(a) and waterfall plot in Fig. 4(c)). For this defect, a shift of LHB away from the Fermi level is observed, as evidenced by a decrease of the LHB maximum in the dI/dV waterfall plot (Fig. 4(c)). Also, the HHB moves toward the Fermi level but to a lesser extent than the LHB and, in consequence, the Mott gap slightly increases, reaching approximately 0.41 eV. The energy shifts of LHB and HHB, as well as the slight opening of Δ_{Mott} can be clearly seen in LHB, HHB, and Δ_{Mott} maps shown in Fig. 3. This allows us to hypothesize that in contrast to D1 which behaves as an acceptor strongly affecting its neighborhood, D4 has donor properties and a much more limited range of influence (i.e., in our experiments, D4 does not appear to substantially impact its direct environment).

Finally, the dI/dV images shown in Fig. 2(d) also reveal one last additional defect, labeled as D5. This defect is characterized by a decrease of TC in the range of −0.09 to −0.18 eV (see dI/dV image recorded at −0.12 eV in Fig. 2(d)). Within this energy range, three CDW sites (indicated with arrows) are surrounded by darker ovals indicative of a reduction of TC. Unfortunately, this defect is difficult to characterize in the plots extracted form D5 CDWs and in dI/dV waterfall plots, and its exact nature is currently unknown. We speculate that either S3 or S4 atoms are affected, leading to a decrease of the TC outside central region of the CDW maximum site. Further experiments performed with finer spatial resolution are required to understand the nature of this defect.

3 DFT analysis

3.1 DFT of defect-free 1T-TaS_2

We now turn to use DFT calculations to gain understanding of the experimental dI/dV data. The reliability of the DFT method is supported by direct comparison of our experimentally recorded ARPES data along the $\bar{\Gamma}-\bar{M}$ direction shown in Figs. 5(a) and 5(b) with the DFT-calculated band structure of single-layer 1T-TaS_2 (Fig. 5(c)). Note, the calculations were carried out using DFT + U formalism [47] (see Methods section, spin up and down bands are indicated using red and blue color, respectively) for the monolayer 1T-TaS_2 supercell, which successfully predicts the PLD responsible for CDW formation (see Fig. 1(b)). In consequence of the extension of the unit cell (supercell is $\left(\sqrt{13}\times\sqrt{13}\right)R_{13.9°}$ in Wood's notation), the 1st Brillouin zone is reduced (see inset in Fig. 1(b)), and therefore, the calculated bands have to be unfolded onto the 1 × 1 Brillouin zone (see Fig. 5(c)) before comparison to ARPES data.

Figures 5(a)–5(c) show the experimental ARPES data and unfolded DFT are in very good agreement. Even bands located as far as 8 eV below the Fermi level are reproduced with high fidelity, despite a slight shift toward the Fermi level in the calculation. We attribute this shift to the calculations done for a single-layer 1T-

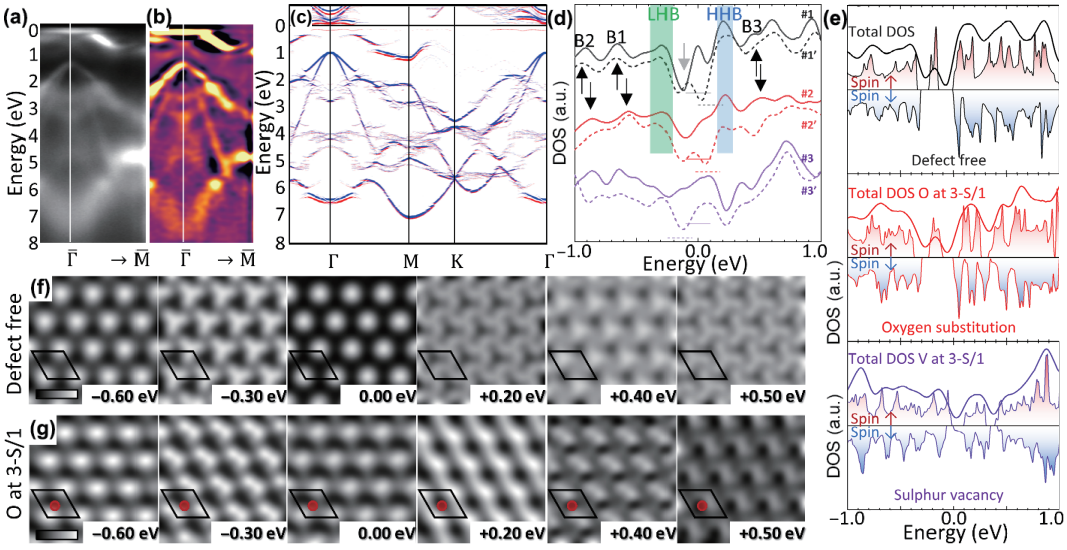

Figure 5 (a) ARPES data measured at 80 K along a $\bar{\Gamma}-\bar{M}$ line in *k* space and (b) its second derivative. (c) Unfolded DFT band structure for 1T-TaS_2 supercell with PLD. Spin up and spin down indicated using red and blue respectively. (d) DFT calculated DOS for defect-free (#1), oxygen substitution (#2), and sulfur vacancy (#3) (see Fig. 1(a) for location of sulfur atom which was substituted and removed). Dashed lines are used to plot DOS calculated using DFT + U. (e) DFT + U calculated spin-polarized DOS and total DOS for (from top) defect free, oxygen substitution, and sulfur vacancy. (f) and (g) DFT calculated LDOS images for defect-free and oxygen substitution respectively. Supercell is indicated in each image. Scale bars in ((f) and (g)) correspond to 1 nm. In (g), 3-S/1 site substituted by oxygen is indicated by the red dot.

TaS_2, while the experiments were carried out on the surface of a bulk 1T-TaS_2 crystal. The band gaps along the $\bar{\Gamma}-\bar{M}$ direction in the energy range below 1.3 eV below the Fermi level are also well reproduced both in experimental and calculated data. These gaps are related to the PLD formation and Coulomb interactions between carriers in 1T-TaS_2. Including a Hubbard term leads to spin-splitting, reaching 0.1 eV for bands at $\bar{M}$ approximate 1.3 eV below the Fermi level and at $\bar{\Gamma}$ close to 7 eV below the Fermi level. Larger spin-splitting is observed above the Fermi level, reaching 0.15 eV (see Fig. 5(c)).

The effect of the Hubbard term on the DOS in the vicinity of the Fermi level is shown in Fig. 5(d), in which the calculated DOS for $U = 0$ and 2.27 eV can be compared (see black plots denoted as #1 and #1', respectively). Both plots are nearly identical, except for the in-gap state shifting below the Fermi level for U = 2.27 eV (indicated by a grey arrow in Fig. 5(d)). The calculated DOS for spin up and spin down are considerably different (see Fig. 5(e)), which is an evidence of magnetic polarization in this system. The calculated total magnetization for 1T-TaS_2 is 0.99 μ_B per supercell, which is equivalent to an excess half-spin per CDW site. Inspection of the calculated DOS in Fig. 5(e) shows a clear band gap of approximate 0.4 eV for spin down. For spin up, a band gap also exists but with a clear fully spin-polarized state in the middle, resulting from spin-splitting of the flat band located at the Fermi level at the Γ point, ignoring Coulomb interactions (see Fig. 5(c)). The spin down band moves up in energy (see first maximum above the Fermi level for spin down in Fig. 5(e)) together with several other bands initially located above the Fermi level form the HHB state. Note, in Fig. 5(e), the Fermi energy is set at the bottom of the conduction band while in Fig. 5(d) DFT + U calculated DOS is shifted by 0.10 eV (p-doped) in order to align the DOS maxima for the $U = 0$ eV case. In both plots, the LHB, HHB, and B1-B3 states are clearly identified (see shaded areas and black arrows in Fig. 5(d)) [33]. These spectral features (see also Fig. S4 in the ESM for on and between CDW LDOS data) are in reasonable agreement with experimental data (Fig. 3(a)) and previously published reports [20, 33]. It is worth underlining here that DFT calculations also indicate a shift in energy of both LHB and HHB. In Fig. S4 in the ESM, we show a comparison of LDOS extracted from the corner of the supercell (centered at A-Ta atom, see Figs. 1(b) and 1(c)) and its center (S4 atom, see Fig. 1(c)). It is evident that the position of LHB and HHB shifts outward the Fermi level leading to the modulation of the Mott band gap.

Our theoretical data show that isolated spin-polarized state should form in 1T-TaS_2 just below the Fermi level. In the experimental data shown in Fig. 3(a), there is no clear signature of such in-gap state. However, we note that the LHB feature fades smoothly towards the band gap as opposed to HHB, which is characterized by a sharper decrease (see Fig. 3(a)). In our opinion, it is possible that this fading of the LHB into the band gap is a signature of the spin-up in-gap state predicted by DFT + U calculations. In consequence, we expect this part of the spectrum to be strongly spin-polarized; this hypothesis could be confirmed or disconfirmed in spin-polarized STM or spin-polarized ARPES measurements.

Our experimental d*I*/d*V* images of the CDW discussed above indicate a strong dependence on the energy (see Fig. 2(d)). Our DFT-calculated LDOS shown in Fig. 5(f) confirms this observation. In order to qualitatively compare these data with STS-recorded d*I*/d*V* images, a Gaussian filtering operation has been performed on the calculated LDOS images to mimic the effect of tip broadening (Fig. S5 in the ESM shows the LDOS images for an energy range of ±1 eV with 0.10 eV interval, and the corresponding smeared versions are shown in Fig. S6 in the ESM). Below the Fermi level, the appearance of the CDW maxima evolves from roughly circular at −0.60 eV to a more triangular arrangement at −0.30 eV. In turn, above the Fermi level, a contrast inversion occurs in particular at the HHB energy (compare −0.3 and +0.20 eV image in Fig. 5(f)). Both lateral shift of CDW maxima and contrast inversion are observed in the experimental data as well (see the description above). Finally, in the experimental STS image obtained at 0.44 eV above the Fermi level, hexagonal rings can be observed with particularly pronounced corners (see Fig. 2(d)). This feature is also reproduced in DFT data for 0.40 and 0.50 eV above the Fermi level, where it is the hollow sites that form a triangular lattice (see Fig. 5(f)).

3.2 Defected 1T-TaS_2

In order to shed some light on defects in single-layer 1T-TaS_2, we decided to simulate sulfur substitution by oxygen and sulfur vacancy as potential point defects (see Fig. S7 in the ESM for

structural models and DOS calculated without Hubbard term; Fig. S8 in the ESM for band diagrams with and without Hubbard term and spin polarized DOS; Fig. S9 in the ESM for band diagrams along path shown in Fig. 1(b) for six point defects). The DFT-calculated DOS for these defects are shown in Fig. 5(d) and are denoted as #2 and #3 respectively. The sulfur atom which we substitute (remove) is indicated by red ring in Fig. 1(a) and denoted as 3-S/1 (see also red dot in Fig. 5(g) and Fig. S7(a) in the ESM for locations of two other S sites for which calculations are performed). Oxygen substitution does not alter the DOS in substantial way. All spectral features, i.e., HHB, LHB, and B1-3 are easily resolved and their location in energy does not substantially change with respect to defect-free 1T-TaS_2. This behavior is in agreement with previous oxidation studies of the 2H-TaS_2 polytype [13]. It is, however, noticeable that for oxidized 1T-TaS_2 the DOS has finite value at the Fermi level, related to the closing of the band gap. This result is independent on the specific site at which oxygen substitution is performed during calculations (three different sites were examined (see DOS in Fig. S7 in the ESM and band diagrams in Fig. S8 in the ESM)).

In contrast, results for DFT + U are heterogeneous and exhibit a significant dependence on the specific substitution site. As shown in the middle panel in Fig. 5(e) and plot #2' in Fig. 5(d), all main electronic features are preserved for oxygen substitution at 3-S/1 site (note plot #2' was shifted toward higher energies by 80 meV to match location of main spectroscopic features) but the band gap remains open (although decreased in comparison to the pristine 1T-TaS_2). Interestingly, different behaviors are observed for the two other oxygen substitution sites (see Figs. S7–S9 in the ESM), where the band gap closes, similar to the case of DFT without Hubbard correction term. In consequence, our results suggest heterogeneity of electronic properties for different oxygen substitution sites. The heterogeneity is also observed in terms of magnetization i.e., for substitution at 3-S/1 site magnetic moment is preserved and equal 1.00 μ_B per supercell while for the two other configurations the magnetic moment is reduced down to 0.17 μ_B per supercell, i.e., by nearly a factor 6.

Based on our calculations, it is hard to predict which of the three examined defects and in consequence which properties will dominate if 1T-TaS_2 undergoes oxidation. The total energy per unit cell is 126 meV lower for 3-S/1 than for other configurations (3-S/2 and 1-S have roughly the same total energy) but calculations were carried out for monolayer with one defect per supercell and, therefore, these results may not be fully quantitative and correspond to the experiments. We can speculate that substantial differences in energies for the different oxygen substitution sites can lead to different scenarios of surface dynamics which may be limited by defect diffusion. To understand this better, larger-scale DFT calculations but also molecular dynamics simulations could be performed.

The observed changes of the DOS for the oxygen substitution case are also clearly visible in LDOS images shown in Fig. 5(g) and Figs. S5 and S6 in the ESM. The CDW modulation is now altered as a direct consequence of layer distortions, shown in Fig. S7 in the ESM. It is also worth to note that introduction of oxygen substitution results in three-fold symmetry breaking, seen in real space, e.g., for +0.20 eV LDOS in Fig. 5(g). In consequence, such defect can be identified experimentally based on local changes in the CDW contrast or shape change during STS experiments.

In contrast to oxygen substitution, the electronic structure for the sulfur vacancies is the same for all three substitution sites. The DOS for a sulfur vacancy at the 3-S/1 site is shown in Fig. 5(d) (see plot #3). It is characterized by a maximum located at the Fermi level, indicative of a metallic behaviour. Moreover, it is characterized by the presence of a DOS minima at the location of LHB (rather subtle) and HHB (much more pronounced). DFT + U calculated DOS is denoted as #3' and shown in Fig. 5(d). It is qualitatively similar to the results obtained without the Hubbard term, with the exception of a semimetallic behaviour (characterized with a very small band gap of approximately 5 μeV; see Fig. 5(e) and Figs. S8 and S9 in the ESM). It is worth mentioning that the spin polarization for sulfur vacancy is relatively large and comparable to defect free 1T-TaS_2 (see bottom panel in Fig. 5(e); total magnetization is 1.00 μ_B per supercell).

The characteristic spectral features for sulfur vacancy remain largely unaffected for other sites in the supercell. Two other sites have been examined and the results of our calculations are shown in Fig. S7 in the ESM. The DOS plots show that they are qualitatively characterized by the same set of spectral features, with little quantitative difference. This is very different to the oxygen substitution case, for which the electronic properties near the Fermi level depend strongly on the specific site.

In order to gain more insight into the physical mechanism of described changes, we show the electronic band structure calculated for a supercell by DFT for defect-free monolayer 1T-TaS_2 and for both defects—oxygen atom and vacancy in three distinct positions: 3-S/1, 3-S/2, and 1-S (see Fig. S8 in the ESM). Note, the presence of defects lowers the symmetry and in consequence the K(M) points in the first Brillouin zone become inequivalent, lifting degeneracies (see Fig. 1(b) and Fig. S8 in the ESM). For defect-free 1T-TaS_2, a flat band is present in the electronic band structure at the Fermi level, originating from the d orbitals of Ta atoms. The inclusion of Hubbard correction (DFT + U) causes the band to spin-split, leaving one of two spin-polarized flat bands in the middle of the band gap (while the second one tends to merge with other bands at higher energy). The energy splitting of the flat band is quite large (the Mott gap opens in the system) and the bandwidth is small, indicating that the system is a Mott insulator [47]. The presence of a sulfur vacancy modifies the electronic structure, as the flat spin-polarized band gains a degree of dispersion (the spin-splitting gap is now indirect) and is pushed down in energy, merging with other bands. This behavior is the same for all three vacancy locations studied here (compare the DOS and energy dispersions along the path indicated in Fig. 1(b) shown Fig. S8 in the ESM, which are nearly identical). It is related to relaxation procedure which drives the system toward identical final structures i.e., deformations around the vacancy are independent on its location within the supercell. The spin-splitting energy is unchanged with respect to the defect-free case. On the contrary, an oxygen substitution at position 3-S/2 or 1-S, leads to enhanced dispersion of the in-gap band, driving the system to metallicity. At the same time, the predicted spin-splitting (and magnetization) is significantly reduced. Oxygen substitution at the 3-S/1 position induces an in-gap, spin-polarized band with narrow dispersion and restored magnetization (qualitatively similar to the defect-free case). This emphasizes the crucial role that defects can play in the electronic properties in this system.

3.3 LDOS in function of distance

To elucidate whether the STM measurements "see" the sulfur or the tantalum atoms, we calculate the LDOS at different distances from the top sulfur plane of 1T-TaS_2. The DFT-calculated LDOS maps are shown in Fig. 6(a), for a distance of −0.1, 0.0, 0.1, 0.2, and 0.8 nm above the top S plane. A negative distance indicates that the LDOS is calculated below the top S plane, i.e., inside the single-layer of 1T-TaS_2. Note, calculations shown in Fig. 6 were conducted for an energy window of 0.1 eV in width, centered at 0.0 eV (i.e., at Fermi level). These data clearly show that LDOS measured above the surface is dominated by sulfur atoms (see equiangular hexagon on the +0.1 nm plane in Fig. 6(a)). The

contribution of the Ta atoms is dominating below the surface, i.e., inside the layer 1T-TaS_2 (David Star at –0.1 nm plane in Fig. 6(a)) and is vanishing above the surface (arrow in Fig. 6(a) indicates weak LDOS associated to A-Ta atom).

The same trend is preserved also for LDOS calculated for different energies. In Fig. 6(b), we show LDOS plotted for A-Ta and 1-S atoms in function of distance and energy. For all energies, high LDOS for A-Ta atom is observed below surface. In turn, above the surface of 1T-TaS_2, S atoms dominate over the Ta atoms in the LDOS.

In order to compare the LDOS measured over A-Ta and 1-S, we evaluate the ratio of both values. Results are shown in Fig. 6(c) as logarithm of 1-S to A-Ta ratio. This plot shows in a clear way that LDOS calculated over 1-S atoms close to the surface is over ten times larger in comparison to LDOS over A-Ta atom. Further away from the surface, the ratio quickly decreases and approaches 1. This is a consequence of the LDOS smearing, associated with the gradual loss of detail in LDOS images as the tip-sample distance increases. In the extreme case of a tip-sample distance of 0.8 nm, the loss of detail is such that the CDW is resolved without any of the details resulting from individual atomic contribution.

3.4 Comparison of DFT results with experimental data

Our experimental data show clear differences between dI/dV plots recorded over the centre of the CDW sites and in-between (see Fig. 3(a)). These differences are reasonably well reproduced by our DFT calculations (see Fig. S4 in the ESM). In particular, a considerably lower LDOS (thus a dI/dV value) is observed between CDW sites in comparison to those obtained over a CDW site. More importantly, in Fig. 3(a) and Fig. S4 in the ESM, a substantial shift of the HHB energy position is observed toward higher energies. The LHB energy position also shifts in our DFT data but more marginally. A similar small shift is also observed experimentally, however in the opposite direction. We believe this discrepancy is a consequence of ignoring inter-layer interactions. Importantly, similarities between experimental and theoretical results indicate that the influence of tip-sample distance on experimental data [48] is negligible in our case. Our results show that the PLD and the associated formation of CDW lead not only to the opening of the band gap but also to periodic modulation of its width commensurate with the PLD. The comparison of our DFT results with experimental measurements allows to initiate discussion on the nature of the point defects resolved by STM/STS. In particular, we find similarities between the DFT-calculated DOS for the sulfur vacancy system and the dI/dV plots obtained on the D2 type of defect. DFT + U is also in very good agreement, although a small energy offset must be used (see Fig. 5(d)) for experimental agreement. The experimental band gap (i.e., global minimum of dI/dV data) is shifted roughly to the location of HHB of defect-free 1T-TaS_2. In consequence, at the Fermi level pronounced maximum is observed at the Fermi level, while weaker local minimum coincides with LHB. A similar DOS is observed for sulfur vacancies which suggests that this is the origin of D2 defects, however, we cannot exclude other possibilities due to qualitative character of our calculations.

Our experimental results show that among all defects investigated experimentally in this study, the D1-type defect impacts the electronic structure of 1T-TaS_2 in a most severe way. We have not been able to reproduce the observed changes of TC in our calculations and therefore we speculate that this defect is related to foreign atoms serving as dopants. Previous studies indeed showed that comparable impacts on the TC can be observed as described here, i.e., shift of HHB and LHB toward the Fermi energy [27, 28] which is a strong argument for the presence of adatom in 1T-TaS_2. Our XPS measurements (not shown) do not evidence the presence of foreign atomic species that could point to the origin of such defect.

The influence of D4 and D5 defects on the electronic structure is very subtle and can be observed only in dI/dV waterfall plots and dI/dV images for certain energies. The origin of these defects is currently unknown. We speculate that D4 is related to donor adatom buried in the crystal. In turn, D5 is probably related to either 3-S or 4-S atoms (see Fig. 1(c)), leading to a decrease of the TC in the close vicinity of the CDW maximum. Further investigations will be necessary to understand the origin and nature of these defects.

We find very large degree of similarity between our ARPES data and band calculations for single layer of 1T-TaS_2 (as shown in Figs. 5(a)–5(c)). This indicates that, in first approximation, results of calculations for single layer can be used to describe properties of multilayer bulk system. We believe this is also holds true when defects are introduced into single layer. To further understand the influence of point defects on the electronic structure of 1T-TaS_2, calculations performed in a multilayer system would be necessary. This would allow to investigate the influence of buried defects like vacancies, substitutions, and intercalations on the global properties

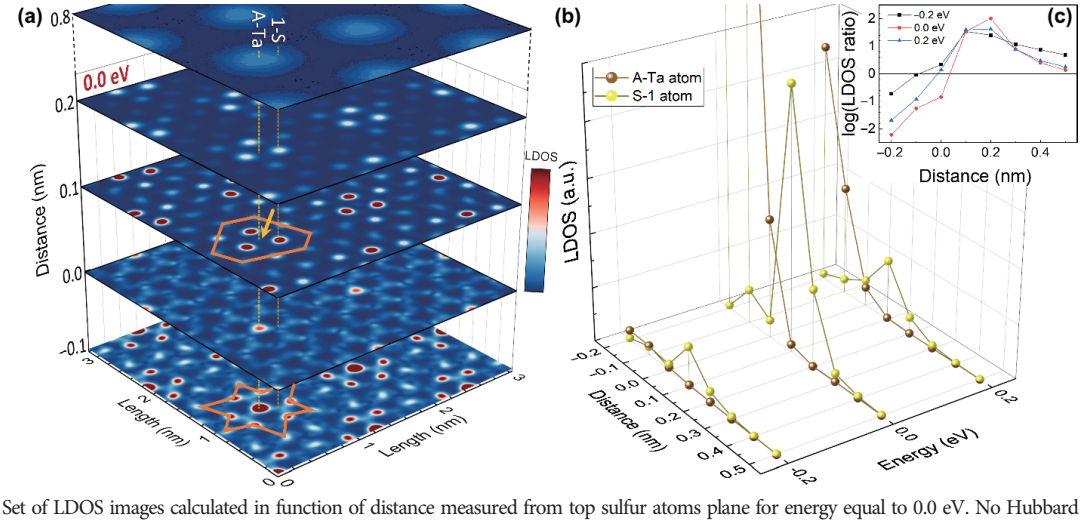

Figure 6 (a) Set of LDOS images calculated in function of distance measured from top sulfur atoms plane for energy equal to 0.0 eV. No Hubbard term is used in calculations. David Star and equiangular hexagon are indicated using orange shapes. A-Ta and 1-S atoms are indicated using dashed line. Scale for 0.8 nm LDOS image is a few hundred times exaggerated in comparison to other images in the plot. (b) Plot of LDOS in function of distance and energy for A-Ta and 1-S atoms. (c) Ratio of LDOS measured over 1-S and A-Ta atoms for energies –0.2, 0.0, and 0.2 eV. Negative distance values indicate that the calculations were performed inside 1T-TaS_2 (under top layer).

of the bulk-like crystal. However, such calculations are highly demanding from a computational viewpoint (the same remark applies to the calculations with lower concentration of defects, requiring much larger supercells). Moreover, the multilayer geometry of the system introduces numerous additional degrees of freedom to be included, like the stacking order of 1T-TaS_2 layers [20, 49] and their polytypes (the subtle interplay of these factors would shape the detailed electronic properties of the system). We believe that the monolayer system computationally investigated here gives at least a qualitative insight into point defects on the properties of 1T-TaS_2, capturing the essential physics of the system.

Finally, in our experiments, we achieve atomically-resolved imaging of the 1T-TaS_2 surface (see Fig. 1(d)). We interpret the observed atomic protrusions originating from the sulfur atoms. This claim is supported by our DFT calculations, depicted in Fig. 6, clearly show that above the 1T-TaS_2 surface, it is the sulfur atoms that mainly contribute to the LDOS within the investigated energy range. The apparent height in the STM images is proportional to the LDOS at constant energy and the largest protrusions in the calculated LDOS are observed above the sulfur atoms. Thus, we believe that in STM experiments it is mainly the top-surface sulfur atoms that are observed. This is supported by the DFT-calculated STM image shown in Fig. 1(e). For larger distances, the subtle details of the atomic resolution are lost, and the image only resolves the CDW periodicity without the details of the atomic structure. Our data also suggest that the LDOS associated with Ta atoms can be detected above surface, in particular the central A-Ta atom. However, LDOS calculated above A-Ta has a Ta-contribution over ten times weaker than the 1-S atom contribution. Nonetheless, we cannot exclude the observation of Ta atoms in STM experiments but in such case we expect that the image would be dominated by the protrusions related to sulfur atoms.

4 Conclusions

In conclusion, we investigated the low-energy electronic properties of 1T-TaS_2 and found that the Mott band gap energy undergoes modulation in record with PLD. We evaluate the impact of structural defects on the 1T-TaS_2 electronic structure, leading to substantial effects both locally and within a radius up to several nanometers. Five types of defects (D1–D5) are identified and their electronic structure is characterized using STS. The D1 defect decreases the Mott gap and behaves as an acceptor, leading to band-bending in a region up to 4–5 nm away of its location. Our results show that few such defects located at some distance result in substantial modulation of the lateral electron density landscape, leading to mutual shifts of the lower and higher Hubbard bands. In contrast, the D2 defect characterized by metallic STS spectra has a limited influence over its neighboring environment, i.e., one CDW site only. Our DFT simulations indicate that D2 is consistent with a sulfur vacancy. The D3 type of defect is characterized by a slight decrease of the Mott band gap and an emergence of additional electronic states below the Fermi energy. The defect D4 is characterized by a slight increase of the Mott gap, however with limited magnitude. These observations clearly indicate that the band gap width depends on the interplay between layer stacking and on the structural defects of the 1T-TaS_2 surface. Finally, the presence of the D5 defect can be spotted within an energy window located approximately 0.12 eV below the Fermi level as a depletion of electronic states around defected CDW sites. All these defects are too subtle to be observed in topographic STM scanning mode. However, the D5 defects become visible when the electronic structure is mapped over an energy range close to the Fermi level. Our experimental observations are supported by DFT calculations, in which the CDW associated with defected supercells is considerably different to the CDW in a defect-free material.

Finally, our DFT calculations show the sensitivity of the electronic structure on the specific oxygen substitution site, with properties either semiconducting and similar to defect free 1T-TaS_2 (open band gap, spin polarized flat band in the gap, magnetization close to 1 μ_B/super cell) or metallic (closed band gap, dispersive band at the Fermi level, quenched magnetic moments). In contrast, the sulfur vacancy site has little impact on the electronic properties (metallic, weakly dispersive bands located above the Fermi level, non-negligible magnetic moments). Clearly, further experimental and theoretical studies are required to understand the role of interlayer interactions, defects, and magnetic properties in 1T-TaS_2.

Overall, the defects observed in this paper shed light on the fragility of the 1T-TaS_2 electronic structure. The electronic perturbations are mainly observed within one, affected CDW site. One exception is the defect working as a dopant, disturbing the electronic structure in range of few nanometers. Such naturally existing defects can considerably affect the global properties of 1T-TaS_2 and their existence should be taken into account if 1T-TaS_2 is considered in future electronic and optoelectronic devices.

5 Methods

The STM/STS measurements (Unisoku Co., USM1400 controlled by Nanonis BP 4.5) were carried out in UHV at 80 K. Typical pressure during measurements was lower than 1×10^{-10} mbar. The STM tips were prepared by mechanical cutting of 90/10 Pt/Ir wires. The $I(V)$ curves were recorded simultaneously with a constant current image by the use of the interrupted-feedback-loop technique. Based on these measurements, the first derivative of the tunneling current with respect to voltage (dI/dV) was calculated numerically.

ARPES measurements were conducted at Polish National Synchrotron SOLARIS at URANOS (former UARPES) beamline, using a DA30L Scienta-Omicron electron spectrometer. The photon energy was set to 67 eV. Sample temperature during measurements was kept at 80 K.

High-quality 1T-TaS_2 crystals were supplied by HQ Graphene and cleaved *in situ* in UHV condition (1×10^{-8} mbar) at room temperature.

First-principles calculations were performed using QUANTUM ESPRESSO suite [50, 51] implementing the DFT formalism with a plane wave basis [52]. The exchange correlation potential of Perdew–Burke–Ernzerhof (PBE) type [53] and projected augmented wave (PAW) approach [54] were utilized, with a kinetic energy cut-off set to 53 Ry. In the calculations, scalar relativistic (DFT + U) and fully relativistic (DFT) pseudopotentials permitting non-collinear calculations with spin–orbit effects were applied [55]. To capture the coulombic correlation effects for the electrons at 5d orbitals of Ta atoms, spin-polarized calculations within DFT + U formalism were performed on the basis of the rotational-invariant approach after Ref. [56]. The Hubbard U value of 2.27 eV was accepted, as derived from linear response-based calculations [26]. To capture the CDW phase in TaS_2, a $\sqrt{13} \times \sqrt{13}$ R13.9° supercell was constructed. For modeling of defected system, a presence of a single defect (sulfur vacancy or substitutional oxygen atom) in a supercell was assumed. In order to model a monolayer system, a slab geometry with at least 15 Å of vacuum separating the periodic images in the direction perpendicular to the layer was used. The 6×6 mesh of k-points was used for relaxation of the atomic positions and self-consistent

calculations, whereas a denser mesh of 24 × 24 (DFT + U) or 48 × 48 (DFT) was applied to non-self-consistent calculations for DOS determination. In the calculations, the vdW correction was applied [57, 58] together with dipole correction introduced in Ref. [59]. The geometry relaxation was performed using a quasi-Newton algorithm. Spatially-resolved LDOS calculations correspond to the plane at constant height of 3 Å over the topmost sulfur atom unless stated otherwise. To permit the comparison of band structures resulting from the supercell-based calculations and from the ARPES measurements, the unfolding procedure from the supercell first Brillouin zone to the normal cell first Brillouin zone was performed with BandUPpy code [60–62]. The simulation of STM image for constant current was performed with CRITIC2 program [63].

Acknowledgments

This work has been supported by the National Science Centre, Poland under grants 2015/19/B/ST3/03142 and 2019/32/T/ST3/00487. M. L. S. thanks for University of Lodz support under IDUB 6/JRR/2021 project. T. -C. C acknowledges support of the U. S. Department of Energy, Office of Science, Office of Basic Energy Sciences, Division of Materials Science and Engineering, under Grant No. DE-FG02-07ER46383. M. G. acknowledges financial support provided by Slovak Research and Development Agency provided under Contract No. APVV-SK-CZ-RD-21-0114 and by the Ministry of Education, Science, Research and Sport of the Slovak Republic provided under Grant No. VEGA 1/0105/20 and Slovak Academy of Sciences project IMPULZ IM-2021-42 and project FLAG ERA JTC 2021 2DSOTECH. Author acknowledges the provision of the Polish Ministry of Education and Science project (Support for research and development with the use of research infrastructure of the National Synchrotron Radiation Centre SOLARIS" under contract nr 1/SOL/2021/2). We acknowledge the SOLARIS Centre for the access to the Beamline URANOS (former UARPES), where the measurements were performed.

Electronic Supplementary Material: Supplementary material (supplementary figures and movies) is available in the online version of this article at https://doi.org/10.1007/s12274-023-5876-7.

References

[1] Hu, Z. H.; Wu, Z. T.; Han, C.; He, J.; Ni, Z. H.; Chen, W. Two-dimensional transition metal dichalcogenides: Interface and defect engineering. *Chem. Soc. Rev.* **2018**, *47*, 3100–3128.

[2] Zhou, M. F.; Wang, W. H.; Lu, J. P.; Ni, Z. H. How defects influence the photoluminescence of TMDCs. *Nano Res.* **2021**, *14*, 29–39.

[3] Liang, Q. J.; Zhang, Q.; Zhao, X. X.; Liu, M. Z.; Wee, A. T. S. Defect engineering of two-dimensional transition-metal dichalcogenides: Applications, challenges, and opportunities. *ACS Nano* **2021**, *15*, 2165–2181.

[4] Ferain, I.; Colinge, C. A.; Colinge, J. P. Multigate transistors as the future of classical metal-oxide-semiconductor field-effect transistors. *Nature* **2011**, *479*, 310–316.

[5] Allen, T. G.; Bullock, J.; Yang, X. B.; Javey, A.; de Wolf, S. Passivating contacts for crystalline silicon solar cells. *Nat. Energy* **2019**, *4*, 914–928.

[6] Chen, Y. Q.; Shu, Z. W.; Zhang, S.; Zeng, P.; Liang, H. K.; Zheng, M. J.; Duan, H. G. Sub-10 nm fabrication: Methods and applications. *Int. J. Extrem. Manuf.* **2021**, *3*, 032002.

[7] Wu, F.; Tian, H.; Shen, Y.; Hou, Z.; Ren, J.; Gou, G. Y.; Sun, Y. B.; Yang, Y.; Ren, T. L. Vertical MoS_2 transistors with sub-1-nm gate lengths. *Nature* **2022**, *603*, 259–264.

[8] Kanungo, S.; Ahmad, G.; Sahatiya, P.; Mukhopadhyay, A.; Chattopadhyay, S. 2D materials-based nanoscale tunneling field effect transistors: Current developments and future prospects. *NPJ 2D Mater. Appl.* **2022**, *6*, 83.

[9] Fiori, G.; Bonaccorso, F.; Iannaccone, G.; Palacios, T.; Neumaier, D.; Seabaugh, A.; Banerjee, S. K.; Colombo, L. Electronics based on two-dimensional materials. *Nat. Nanotechnol.* **2014**, *9*, 768–779.

[10] Akinwande, D.; Huyghebaert, C.; Wang, C. H.; Serna, M. I.; Goossens, S.; Li, L. J.; Wong, H. S. P.; Koppens, F. H. L. Graphene and two-dimensional materials for silicon technology. *Nature* **2019**, *573*, 507–518.

[11] Mak, K. F.; Shan, J. Photonics and optoelectronics of 2D semiconductor transition metal dichalcogenides. *Nat. Photonics* **2016**, *10*, 216–226.

[12] Tan, T.; Jiang, X. T.; Wang, C.; Yao, B. C.; Zhang, H. 2D material optoelectronics for information functional device applications: Status and challenges. *Adv. Sci.* **2020**, *7*, 2000058.

[13] Bekaert, J.; Khestanova, E.; Hopkinson, D. G.; Birkbeck, J.; Clark, N.; Zhu, M. J.; Bandurin, D. A.; Gorbachev, R.; Fairclough, S.; Zou, Y. C. et al. Enhanced superconductivity in few-layer TaS_2 due to healing by oxygenation. *Nano Lett.* **2020**, *20*, 3808–3818.

[14] Rossnagel, K. On the origin of charge-density waves in select layered transition-metal dichalcogenides. *J. Phys. :Condens. Matter* **2011**, *23*, 213001.

[15] Han, T. R. T.; Zhou, F. R.; Malliakas, C. D.; Duxbury, P. M.; Mahanti, S. D.; Kanatzidis, M. G.; Ruan, C. Y. Exploration of metastability and hidden phases in correlated electron crystals visualized by femtosecond optical doping and electron crystallography. *Sci. Adv.* **2015**, *1*, e1400173.

[16] Wang, W.; Dietzel, D.; Schirmeisen, A. Lattice discontinuities of 1T-TaS_2 across first order charge density wave phase transitions. *Sci. Rep.* **2019**, *9*, 7066.

[17] Wang, Y. D.; Yao, W. L.; Xin, Z. M.; Han, T. T.; Wang, Z. G.; Chen, L.; Cai, C.; Li, Y.; Zhang, Y. Band insulator to Mott insulator transition in 1T-TaS_2. *Nat. Commun.* **2020**, *11*, 4215.

[18] Jiang, T.; Hu, T.; Zhao, G. D.; Li, Y. C.; Xu, S. W.; Liu, C.; Cui, Y. N.; Ren, W. Two-dimensional charge density waves in TaX_2 (X = S, Se, Te) from first principles. *Phys. Rev. B* **2021**, *104*, 075147.

[19] Klanjšek, M.; Zorko, A.; Žitko, R.; Mravlje, J.; Jagličić, Z.; Biswas, P. K.; Prelovšek, P.; Mihailovic, D.; Arčon, D. A high-temperature quantum spin liquid with polaron spins. *Nat. Phys.* **2017**, *13*, 1130–1134.

[20] Butler, C. J.; Yoshida, M.; Hanaguri, T.; Iwasa, Y. Mottness versus unit-cell doubling as the driver of the insulating state in 1T-TaS_2. *Nat. Commun.* **2020**, *11*, 2477.

[21] Ma, L. G.; Ye, C.; Yu, Y. J.; Lu, X. F.; Niu, X. H.; Kim, S.; Feng, D. L.; Tománek, D.; Son, Y. W.; Chen, X. H.; et al. A metallic mosaic phase and the origin of Mott-insulating state in 1T-TaS_2. *Nat. Commun.* **2016**, *7*, 10956.

[22] Stojchevska, L.; Vaskivskyi, I.; Mertelj, T.; Kusar, P.; Svetin, D.; Brazovskii, S.; Mihailovic, D. Ultrafast switching to a stable hidden quantum state in an electronic crystal. *Science* **2014**, *344*, 177–180.

[23] Vaskivskyi, I.; Gospodaric, J.; Brazovskii, S.; Svetin, D.; Sutar, P.; Goreshnik, E.; Mihailovic, I. A.; Mertelj, T.; Mihailovic, D.

Controlling the metal-to-insulator relaxation of the metastable hidden quantum state in 1T-TaS_2. *Sci. Adv.* **2015**, *1*, e1500168.
[24] Stahl, Q.; Kusch, M.; Heinsch, F.; Garbarino, G.; Kretzschmar, N.; Hanff, K.; Rossnagel, K.; Geck, J.; Ritschel, T. Collapse of layer dimerization in the photo-induced hidden state of 1T-TaS_2. *Nat. Commun.* **2020**, *11*, 1247.
[25] Zong, A.; Shen, X. Z.; Kogar, A.; Ye, L. D.; Marks, C.; Chowdhury, D.; Rohwer, T.; Freelon, B.; Weathersby, S.; Li, R. K. et al. Ultrafast manipulation of mirror domain walls in a charge density wave. *Sci. Adv.* **2018**, *4*, eaau5501.
[26] Lacinska, E. M.; Furman, M.; Binder, J.; Lutsyk, I.; Kowalczyk, P. J.; Stepniewski, R.; Wysmolek, A. Raman optical activity of 1T-TaS_2. *Nano Lett.* **2022**, *22*, 2835–2842.
[27] Gao, J. J.; Zhang, W. H.; Si, J. G.; Luo, X.; Yan, J.; Jiang, Z. Z.; Wang, W.; Lv, H. Y.; Tong, P.; Song, W. H. et al. Chiral charge density waves induced by Ti-doping in 1T-TaS_2. *Appl. Phys. Lett.* **2021**, *118*, 213105.
[28] Zhang, W. H.; Gao, J. J.; Cheng, L.; Bu, K. L.; Wu, Z. X.; Fei, Y.; Zheng, Y.; Wang, L.; Li, F. S.; Luo, X. et al. Visualizing the evolution from Mott insulator to Anderson insulator in Ti-doped 1T-TaS_2. *NPJ Quantum Mater.* **2022**, *7*, 8.
[29] Liu, Y.; Ang, R.; Lu, W. J.; Song, W. H.; Li, L. J.; Sun, Y. P. Superconductivity induced by Se-doping in layered charge-density-wave system 1T-$TaS_{2-x}Se_x$. *Appl. Phys. Lett.* **2013**, *102*, 192602.
[30] Zhao, Y.; Nie, Z. W.; Hong, H.; Qiu, X.; Han, S. Y.; Yu, Y.; Liu, M. X.; Qiu, X. H.; Liu, K. H.; Meng, S. et al. Spectroscopic visualization and phase manipulation of chiral charge density waves in 1T-TaS_2. *Nat. Commun.* **2023**, *14*, 2223.
[31] Ishioka, J.; Liu, Y. H.; Shimatake, K.; Kurosawa, T.; Ichimura, K.; Toda, Y.; Oda, M.; Tanda, S. Chiral charge-density waves. *Phys. Rev. Lett.* **2010**, *105*, 176401.
[32] Yu, X. L.; Liu, D. Y.; Quan, Y. M.; Wu, J. S.; Lin, H. Q.; Chang, K.; Zou, L. J. Electronic correlation effects and orbital density wave in the layered compound 1T-TaS_2. *Phys. Rev. B* **2017**, *96*, 125138.
[33] Lutsyk, I.; Rogala, M.; Dabrowski, P.; Krukowski, P.; Kowalczyk, P. J.; Busiakiewicz, A.; Kowalczyk, D. A.; Lacinska, E.; Binder, J.; Olszowska, N. et al. Electronic structure of commensurate, nearly commensurate, and incommensurate phases of 1T-TaS_2 by angle-resolved photoelectron spectroscopy, scanning tunneling spectroscopy, and density functional theory. *Phys. Rev. B* **2018**, *98*, 195425.
[34] Song, X.; Liu, L. W.; Chen, Y. Y.; Yang, H.; Huang, Z. P.; Hou, B. F.; Hou, Y. H.; Han, X.; Yang, H. X.; Zhang, Q. Z. et al. Atomic-scale visualization of chiral charge density wave superlattices and their reversible switching. *Nat. Commun.* **2022**, *13*, 1843.
[35] Luican-Mayer, A.; Zhang, Y.; DiLullo, A.; Li, Y.; Fisher, B.; Ulloa, S. E.; Hla, S. W. Negative differential resistance observed on the charge density wave of a transition metal dichalcogenide. *Nanoscale* **2019**, *11*, 22351–22358.
[36] Hla, S. W.; Marinković, V.; Prodan, A.; Muševič, I. STM/AFM investigations of β-$MoTe_2$, α-$MoTe_2$ and WTe_2. *Surf. Sci.* **1996**, *352–354*, 105–111.
[37] Spera, M.; Scarfato, A.; Pásztor, Á.; Giannini, E.; Bowler, D. R.; Renner, C. Insight into the charge density wave gap from contrast inversion in topographic STM images. *Phys. Rev. Lett.* **2020**, *125*, 267603.
[38] Pásztor, Á.; Scarfato, A.; Spera, M.; Flicker, F.; Barreteau, C.; Giannini, E.; van Wezel, J.; Renner, C. Multiband charge density wave exposed in a transition metal dichalcogenide. *Nat. Commun.* **2021**, *12*, 6037.
[39] Hu, Y. N.; Zhang, T. Z.; Zhao, D. M.; Chen, C.; Ding, S. Y.; Yang, W. T.; Wang, X.; Li, C. H.; Wang, H. T.; Feng, D. L. et al. Real-space observation of incommensurate spin density wave and coexisting charge density wave on Cr(001) surface. *Nat. Commun.* **2022**, *13*, 445.
[40] N'Diaye, A. T.; Coraux, J.; Plasa, T. N.; Busse, C.; Michely, T. Structure of epitaxial graphene on Ir(111). *New J. Phys.* **2008**, *10*, 043033.
[41] Aishwarya, A.; Raghavan, A.; Howard, S.; Cai, Z. Z.; Thakur, G. S.; Won, C.; Cheong, S. W.; Felser, C.; Madhavan, V. Long-lifetime spin excitations near domain walls in 1T-TaS_2. *Proc. Natl. Acad. Sci. USA* **2022**, *119*, e2121740119.
[42] Odds, F. C. Spirolaterals. *Math. Teach.* **1973**, *66*, 121–124.
[43] Cho, D.; Gye, G.; Lee, J.; Lee, S. H.; Wang, L. H.; Cheong, S. W.; Yeom, H. W. Correlated electronic states at domain walls of a Mott-charge-density-wave insulator 1T-TaS_2. *Nat. Commun.* **2017**, *8*, 392.
[44] Chen, Y.; Ruan, W.; Wu, M.; Tang, S. J.; Ryu, H.; Tsai, H. Z.; Lee, R. L.; Kahn, S.; Liou, F.; Jia, C. H. et al. Strong correlations and orbital texture in single-layer 1T-$TaSe_2$. *Nat. Phys.* **2020**, *16*, 218–224.
[45] Liu, M. K.; Leveillee, J.; Lu, S. Z.; Yu, J.; Kim, H.; Tian, C.; Shi, Y. G.; Lai, K. J.; Zhang, C. D.; Giustino, F. et al. Monolayer 1T-$NbSe_2$ as a 2D-correlated magnetic insulator. *Sci. Adv.* **2021**, *7*, eabi6339.
[46] Shah, A.; Munshi, A. H.; Nicholson, A. P.; Thiyagarajan, A.; Pozzoni, U. M.; Sampath, W. S. Atomistic modeling of energy band alignment in CdSeTe surfaces. *Appl. Surf. Sci.* **2021**, *544*, 148762.
[47] Darancet, P.; Millis, A. J.; Marianetti, C. A. Three-dimensional metallic and two-dimensional insulating behavior in octahedral tantalum dichalcogenides. *Phys. Rev. B* **2014**, *90*, 45134.
[48] Kohsaka, Y.; Taylor, C.; Fujita, K.; Schmidt, A.; Lupien, C.; Hanaguri, T.; Azuma, M.; Takano, M.; Eisaki, H.; Takagi, H. et al. An intrinsic bond-centered electronic glass with unidirectional domains in underdoped cuprates. *Science* **2007**, *315*, 1380–1385.
[49] Wu, Z. X.; Bu, K. L.; Zhang, W. H.; Fei, Y.; Zheng, Y.; Gao, J. J.; Luo, X.; Liu, Z.; Sun, Y. P.; Yin, Y. Effect of stacking order on the electronic state of 1T-TaS_2. *Phys. Rev. B* **2022**, *105*, 035109.
[50] Giannozzi, P.; Baroni, S.; Bonini, N.; Calandra, M.; Car, R.; Cavazzoni, C.; Ceresoli, D.; Chiarotti, G. L.; Cococcioni, M.; Dabo, I. et al. QUANTUM ESPRESSO: A modular and open-source software project for quantum simulations of materials. *J. Phys.: Condens. Matter* **2009**, *21*, 395502.
[51] Giannozzi, P.; Andreussi, O.; Brumme, T.; Bunau, O.; Buongiorno Nardelli, M.; Calandra, M.; Car, R.; Cavazzoni, C.; Ceresoli, D.; Cococcioni, M. et al. Advanced capabilities for materials modelling with quantum ESPRESSO. *J. Phys. :Condens. Matter* **2017**, *29*, 465901.
[52] Hohenberg, P.; Kohn, W. Inhomogeneous electron gas. *Phys. Rev.* **1964**, *136*, B864–B871.
[53] Perdew, J. P.; Burke, K.; Ernzerhof, M. Generalized gradient approximation made simple. *Phys. Rev. Lett.* **1996**, *77*, 3865–3868.
[54] Kresse, G.; Joubert, D. From ultrasoft pseudopotentials to the projector augmented-wave method. *Phys. Rev. B* **1999**, *59*, 1758–1775.
[55] Dal Corso, A. Pseudopotentials periodic table: From H to Pu. *Comput. Mater. Sci.* **2014**, *95*, 337–350.
[56] Cococcioni, M.; de Gironcoli, S. Linear response approach to the calculation of the effective interaction parameters in the LDA + U method. *Phys. Rev. B* **2005**, *71*, 035105.
[57] Grimme, S. Semiempirical GGA-type density functional constructed with a long-range dispersion correction. *J. Comput. Chem.* **2006**, *27*, 1787–1799.
[58] Barone, V.; Casarin, M.; Forrer, D.; Pavone, M.; Sambi, M.; Vittadini, A. Role and effective treatment of dispersive forces in materials: Polyethylene and graphite crystals as test cases. *J. Comput. Chem.* **2009**, *30*, 934–939.
[59] Bengtsson, L. Dipole correction for surface supercell calculations. *Phys. Rev. B* **1999**, *59*, 12301–12304.
[60] Medeiros, P. V. C.; Tsirkin, S. S.; Stafström, S.; Björk, J. Unfolding spinor wave functions and expectation values of general operators: Introducing the unfolding-density operator. *Phys. Rev. B* **2015**, *91*, 041116(R).
[61] Medeiros, P. V. C.; Stafström, S.; Björk, J. Effects of extrinsic and intrinsic perturbations on the electronic structure of graphene: Retaining an effective primitive cell band structure by band unfolding. *Phys. Rev. B* **2014**, *89*, 041407(R).
[62] Iraola, M.; Mañes, J. L.; Bradlyn, B.; Horton, M. K.; Neupert, T.; Vergniory, M. G.; Tsirkin, S. S. IrRep: Symmetry eigenvalues and irreducible representations of *ab initio* band structures. *Comput. Phys. Commun.* **2022**, *272*, 108226.
[63] Otero-de-la-Roza, A.; Johnson, E. R.; Luaña, V. Critic2: A program for real-space analysis of quantum chemical interactions in solids. *Comput. Phys. Commun.* **2014**, *185*, 1007–1018.